Check for updates

Batteries & Supercaps

Research Article
doi.org/10.1002/batt.202300041

Chemistry Europe
European Chemical Societies Publishing

www.batteries-supercaps.org

Accelerated Workflow for Antiperovskite-based Solid State Electrolytes

Benjamin H. Sjølin,[a] Peter B. Jørgensen,[a] Andrea Fedrigucci,[a, b] Tejs Vegge,[a] Arghya Bhowmik,*[a] and Ivano E. Castelli*[a]

We developed and implemented a multi-target multi-fidelity workflow to explore the chemical space of antiperovskite materials with general formula X_3BA (X=Li, Na, Mg) and Pm-3m space group, searching for stable high-performance solid state electrolytes for all-solid state batteries. The workflow is based on the calculation of thermodynamic and kinetic properties, including phase and electrochemical stability, semiconducting behavior, and ionic diffusivity. To accelerate calculation of the kinetic properties, we use a surrogate model to predict the transition state structure during ionic diffusion. This reduces the calculation cost by more than one order of magnitude while keeping the mean error within 73 meV of the more accurate nudged elastic band method. This method identifies 14 materials that agree with the experimentally reported results as some of the best solid state electrolytes. Moreover, this approach is general and chemistry neutral, so can be applied to other battery chemistries and crystal prototypes.

Introduction

Solid state batteries (SSBs) are some of the most promising alternatives to secondary batteries, which are based on liquid, flammable electrolytes. SSBs are safe, as the flammable liquid is replaced by non-volatile solid components.[1] Moreover, they show improved energy density and cycling life. However, three limitations need to be solved before SSBs can replace their liquid electrolyte counterparts:[2] 1) the ionic conductivity of the solid state electrolytes (SSEs) must be improved to fabricate batteries with high power density;[3] 2) the electrochemical stability window must be widened, such that the SSEs are stable towards high voltage cathodes (e.g., >5 V vs. Li/Li^+, for Li-ion batteries) and metallic anodes;[4] 3) the interface resistance between the SSE and the electrodes must be reduced.[1,5]

A variety of SSEs have been discovered and tested.[6] The first SSE for Li-ion batteries was $Li_{2+2x}Zn_{1-x}GeO_4$ (LISICON family), which showed low ionic conductivity[7] and limited electrochemical stability.[8] $LiAlTiPO_4$ (LATP)[9] and perovskites (typically titanates)[10] represent an improvement over LISICON in terms of ionic conductivity. However, their stability window is similar to that of LISICON[8] and they are affected by the reduction of Ti^{4+} to Ti^{3+}, which gives rise to an undesired increase in electronic conductivity.[11] So far, the best SSE Li-ion conductors are sulfides, such as $Li_{10}GeP_2S_{12}$ (LGPS), which show conductivities close to those of conventional liquid electrolytes at room temperature.[4] However, these sulfides are not stable in the ambient atmosphere, reacting with moisture to form hydrogen sulfide, which is a highly flammable and explosive gas. Nevertheless, efforts have not only been focused on improving the ionic conductivity of solid electrolytes, but also on increasing the electrochemical stability window. In this regard, the amorphous LIPON[12] and garnets[13] display stability windows beyond 3.5 V, but their ionic conductivities are as low as that of LISICON. Similarly, SSEs have been designed for other battery chemistries, such as Na- and Mg-ion batteries, showing similar limitations as for Li-ion batteries.[14,15] Despite these and other studies, the ideal SSE, with both high ionic conductivity and electrochemical stability, remains elusive. Since materials engineering focused on one property might compromise another, the continued search for SSEs needs to be multi-targeted, such that all required properties are met simultaneously.

Recently a new class of materials, denoted charge inverted crystals, have shown exceptional properties.[16] They are obtained by swapping positive and negative ions in the crystal structure of ordinary crystals, and are known to have exceptional properties, such as superionic-[17] and superconductivity,[18,19] massive magnetoresistance,[20] negative thermal expansion,[21] luminescence,[22] and electrochemical energy conversion.[23]

Antiperovskites, which are the charge inverted version of perovskites, have the general formula X_3BA and are formed by two anions (A and B) and three cations (X)[16] as shown in

[a] B. H. Sjølin, Dr. P. B. Jørgensen, A. Fedrigucci, Prof. T. Vegge, Dr. A. Bhowmik, Prof. I. E. Castelli
Department of Energy Conversion and Storage
Technical University of Denmark (DTU)
Anker Engelunds Vej, Building 301, 2800 Kgs. Lyngby (Denmark)
E-mail: arbh@dtu.dk
ivca@dtu.dk

[b] A. Fedrigucci
Theory and Simulation of Materials
École Polytechnique Fédérale de Lausanne
Station 9, CH-1015 Lausanne (Switzerland)

An invited contribution to a Special Collection dedicated to NordBatt 2022 conference.

© 2023 The Authors. Batteries & Supercaps published by Wiley-VCH GmbH. This is an open access article under the terms of the Creative Commons Attribution Non-Commercial License, which permits use, distribution and reproduction in any medium, provided the original work is properly cited and is not used for commercial purposes.

© 2023 The Authors. Batteries & Supercaps published by Wiley-VCH GmbH

Research Article
doi.org/10.1002/batt.202300041
Chemistry Europe
European Chemical Societies Publishing

Figure 1. In relation to SSEs, antiperovskites such as Li_3OCl and Li_3OBr show promising properties, such as relatively high Li-conductivity at medium temperatures, and they can decompose into benign compounds in water.[24]

Computer simulations, especially within the framework of Density Functional Theory (DFT), have been successfully used to discover novel materials with improved properties.[25] This approach uses descriptors, which link calculated microscopic quantities with the measured, macroscopic properties of materials. Examples are total energies for stability, band gaps for light harvesting efficiency, and diffusion barriers for ionic conductivity. The calculations of these descriptors are often organized in computational workflows, which concatenate the calculations and implement corrective strategies for common computational errors.

A few recent examples of computational workflows implemented for battery applications[26] are workflows based on thermodynamic and kinetic properties to discover intercalation electrodes,[27] and new SSEs.[28] Generally, the calculation of thermodynamic properties take significantly less time and resources than the calculations needed to estimate kinetic properties, which are often based on the estimation of ionic diffusion barriers using the Nudged Elastic Band (NEB) method.[29] NEB methods require many DFT simulations to calculate energy/forces, since a number of internal images (intermediate structures) between two fixed end points are optimized over many cycles to find an appropriate saddle point. To avoid image effects, a supercell approach is required for NEB calculations, further increasing the computational cost due to cubic scaling of DFT to the system size. Therefore, traditional DFT based NEB is not appropriate for large scale screening studies for materials discovery.

Different methods have been proposed to accelerate NEB simulations, which include methods that reduce the number of images to calculate, for example, using crystal symmetries,[30] machine learning to identify the transition state (TS),[31,32] or Gaussian process regression for fast barriers.[33]

Fast screening for highly diffusive materials is achievable with less accurate models that still capture trends, with the use of charge density based descriptors having emerged recently.[28,34–37] The underlying chemical understanding behind these models is that the fully charged cations can move through a host lattice containing anions of highly electronegative character without influencing the valence electronic charge density of the framework.[34] These models generally probe the local electrostatic interaction energy with either a point charge[28,34] or finite sized ion model[36] and through this create a surrogate model for the ionic diffusion as an alternative to DFT based NEB or Ab-initio Molecular Dynamics (AIMD). While principled surrogate electrostatics driven models provide fairly accurate estimation of diffusion barriers when parameterized,[28,34] simple topological analysis of the charge density of the host lattice can provide approximate diffusion pathways. These pathways connect the intercalation sites along the low charge density valley while avoiding high charge density regions found near the anions. Thus, one can optimize a pathway between two points in the charge density by running a NEB algorithm using the electronic charge density as a static potential.[35,37]

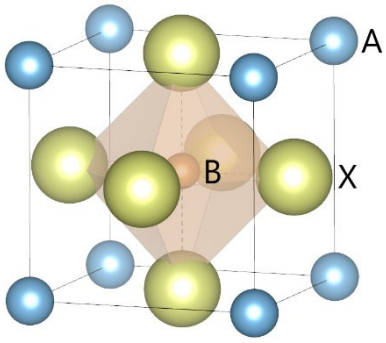

Figure 1. The general structure of antiperovskites with formula X_3BA and space group Pm-3m.

Acquiring the charge density requires only a single DFT self-consistent calculation (SCF), so obtaining the diffusion paths is exceptionally inexpensive with this approach compared to the traditional methods.

In this paper, we introduce a workflow to discover SSEs, encompassing multiple design criteria for electronic, thermodynamic, kinetic and electrochemical properties while utilizing both high-fidelity quantum mechanical models and low fidelity surrogate models to achieve computational efficiency.

We solve the most critical bottleneck, the time-consuming NEB calculations, by implementing a surrogate model able to identify the TS allowing the replacement of NEB simulations with only two DFT calculations. Although principally applicable to any crystal structure, we use this workflow to study the antiperovskite class and identify a handful of candidate materials for SSEs.

Computational Methods

Workflow

To accelerate the discovery of novel SSE materials, we have arranged the calculations in a filtering workflow. Inspired by our previous workflow for intercalation electrodes,[27] the workflow is implemented in the framework of the MyQueue workflow engine,[38] uses the Atomistic Simulation Environment (ASE) to handle crystal structures,[39] and VASP as the simulation engine to run the DFT calculations.[40,41] The workflow is general and can be adapted to any crystal structure.

The structure of the antiperovskites examined in this work corresponds to the cubic Pm-3m space group as illustrated in Figure 1. We limit ourselves to antiperovskites containing Li, Na, and Mg in the X-ion position, since these cations are the currently most studied battery chemistries. The A- and B-ion positions have been filled according to Figure 2 for a total number of compounds under examination of 1317, given that X, A, and B must be unique.

Although the chosen space group disallows reproduction of distortions, such as octahedral tilting, the five-atom unit cell

© 2023 The Authors. Batteries & Supercaps published by Wiley-VCH GmbH

25666223, 2023, 6, Downloaded from https://chemistry-europe.onlinelibrary.wiley.com/doi/10.1002/batt.202300041 by University of Ulsan, Wiley Online Library on [11/11/2025]. See the Terms and Conditions (https://onlinelibrary.wiley.com/terms-and-conditions) on Wiley Online Library for rules of use; OA articles are governed by the applicable Creative Commons License

Research Article
doi.org/10.1002/batt.202300041
Chemistry Europe
European Chemical Societies Publishing

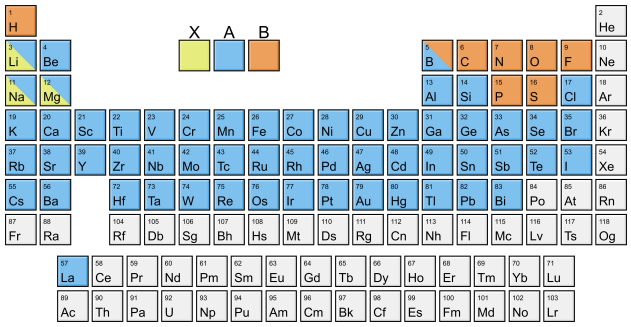

Figure 2. The compositional space for the antiperovskites examined in this study. Since we are examining SSEs, we have restricted X to Li, Na, and Mg. For any compound X, A, and B must be unique.

allows for fast screening of the large chemical space.[42] This leaves a potential investigation of distortions to the handful of candidate materials resulting from the cubic screening. We note that this approach could generate false-positives and -negatives, but we aim at limiting the risk of false-negatives by considering less restrictive filtering criteria.

The workflow employed in this study is outlined in Figure 3. The computational load is balanced, since computational cost increases at each step of the workflow, while the number of compounds examined decreases. Compounds are rejected at each step, based on the criteria at that point in the funnel. The inset in the funnel is the method developed for accelerating the calculations of the diffusion barriers, and it is discussed later in the sections Surrogate NEB and Nudged Elastic Band on Charge Density.

Structural relaxations

The structural relaxations are performed at the DFT-level using the VASP package. Exchange and correlation effects are approximated using the Perdew-Burke-Ernzerhof (PBE) Generalized Gradient Approximation (GGA) functional,[43] using an energy cut-off of 520 eV. The pseudopotentials used are the *materialsproject* set in the ASE-VASP interface, which makes the calculations commensurate to those of The Materials Project.[44] For the unit cell relaxations a k-point grid of 7×7×7 is used, with a grid of 4×4×4 for the supercells, both being Gamma-centered. The structures are relaxed in both atomic positions and unit cell such that the maximum of the residual forces is 0.02 eV/Å using a Conjugate Gradient (CG) algorithm with no symmetry considerations. The atomic positions are initially rattled with a standard deviation of 0.01 Å, and partial orbital occupancy is treated through Gaussian smearing with width 0.05 eV.

To ensure a high and constant resolution of the output charge density, contained in the CHGCAR file, the VASP parameters NG(X/Y/Z) are fixed at 50.

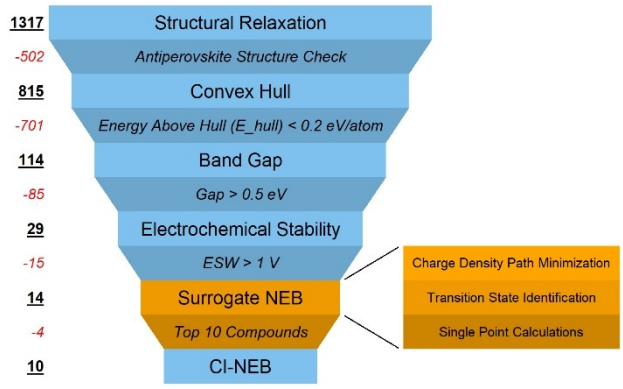

Figure 3. A visualization of the steps in the workflow, along with the filtering criteria used to lower the total computational cost of the screening. The underscored and italic numbers represent the number of compounds present at each step and the number lost to each criterion, respectively. The inset illustrates the steps of the S-NEB method.

Antiperovskite structure check

The first filtering criteria is needed since the relaxations alter both the unit cell and atomic positions, which yields deviations from the ideal Pm-3m space group. To verify that the crystal structure is still close to the Pm-3m space group, each structure must comply with the following 5 criteria, and are otherwise rejected:

1. Unit cell angles are 90 ± 2°.
2. Unit cell lengths are within 0.5 Å of each other.
3. X-A distances are within 0.5 Å of each other.
4. X-B distances are within 0.5 Å of each other.
5. Octahedral angles are 90 ± 13°.

Thermodynamic stability

The thermodynamic stability of each compound is assessed via its energy above the convex hull, which is determined using the *phase_diagram* module of the *pymatgen* python package.[45,46] The convex hull defines the stability frontier from the most stable crystal structures, based on formation energy, within the chemical space of the compound.

A compound is considered thermodynamically stable if its formation energy is below the convex hull, in which case it conforms to the filtering criteria.

Due to the inaccuracies of DFT energies, possible kinetic stability, and metastability, we relax the criteria to include compounds with an energy above the hull of less than 0.2 eV/at. This value aligns with the metastability threshold for the synthesizability of polymorphs.[42,47,48]

Electronic properties

Electrolytes must have minimal electronic conductivity, otherwise they will short out the cell. Therefore, a compound must be either a semiconductor or an insulator to be considered for use as an electrolyte. Both semiconductors and insulators are characterized by their discernible band gap.

© 2023 The Authors. Batteries & Supercaps published by Wiley-VCH GmbH

25666223, 2023, 6, Downloaded from https://chemistry-europe.onlinelibrary.wiley.com/doi/10.1002/batt.202300041 by University of Ulsan, Wiley Online Library on [11/11/2025]. See the Terms and Conditions (https://onlinelibrary.wiley.com/terms-and-conditions) on Wiley Online Library for rules of use; OA articles are governed by the applicable Creative Commons License

Research Article
doi.org/10.1002/batt.202300041
Chemistry Europe
European Chemical Societies Publishing

PBE is used to determine the band gap, yielding a low computational cost, even though PBE is known to underestimate band gaps.[49] The band gap is estimated as the difference between two k-point energies obtained from the relaxations, where the two k-points are: 1) the highest energy k-point of the last occupied band, 2) the lowest energy k-point of the first unoccupied band. We assume that the k-points approximately match those of the actual gap. Therefore, the gap difference to a band structure calculation should be sufficiently small. This is a cheap way to differentiate between conductive and insulating species as it uses the already computed data from the relaxations.

One should expect there to be a small fraction of compounds that get mislabeled using this approximate method. In this study, a cut-off band gap of 0.5 eV is used to differentiate between conductive and insulating materials, which should allow only insulators through this filter.

Electrochemical stability

The Electrochemical Stability Window (ESW) is measured in relation to an electrochemically active pair. In this study, the active pairs are Li/Li^+, Na/Na^+, and Mg/Mg^{2+}, depending on the compound. Determination of the ESW can be achieved using Grand Potential Phase Diagrams (GPPDs),[8,45,50] which entails varying the electrochemical potential of the relevant element. The range of potentials, where the compound lies on the convex hull for that electrochemical potential range, is the ESW of the compound.

It has been found that the decomposition of antiperovskites into their alkali metal oxides is generally kinetically inhibited,[51] so these oxides have been excluded from the ESW calculations. Excluding these results in a wider ESW, which is likely closer to the experimental ESW, since the thermodynamically favorable decomposition into alkali metal oxide would not occur experimentally due to kinetics.[51]

Additionally, a material must lie on the convex hull for the ESW to be computable, so the DFT energies are artificially reduced by an amount equal to the computed energy above the hull in eV/at, rounded up to 2 decimals. Therefore, the GPPDs herein generally relate to metastable phase diagrams.

A minimal ESW of 1 V is chosen as the passing criteria, being just large enough to allow practical SSE usage. Thus, compounds with an ESW smaller than 1 V are rejected.

It should be noted that both the band gap and the ESW calculated herein relate to antiperovskites with no X-ion vacancies, which does not fully represent how they are measured and used experimentally. Performing the screening on more accurate compositions, i.e., with X-ion vacancies, is very important for the band gap and ESW, as explained by Binninger et al.,[52] but due to the large increase in computational cost, we only examine these properties from the standpoint of small non-vacant unit cells.

Migration Barriers

Surrogate NEB

Ionic conductivity is usually determined using NEB methods,[27] but in this study, we propose a surrogate method for this to accelerate these calculations. We call the method Surrogate NEB (S-NEB), as it uses a NEB procedure on the static charge density (contained in the CHGCAR file) of the relaxed structure to determine the TS of the static structure. The NEB part of the method is described in Nudged Elastic Band on Charge Density.

Using NEB on the charge density yields the estimated TS, and a barrier estimate based on the charge density, denoted CD, which does not correlate with the migration barrier as shown in Results and Discussion. Then, the obtained TS is used to estimate the migration barrier through two DFT SCF vacancy calculations, with one having a vacant X-site (Figure 4a) and the other being the identified TS (Figure 4b).

Both supercells are $2\times2\times2$, neither of which are re-relaxed. The estimate of the migration barrier, E^{+}_{S}, is the energy difference between these two supercells.

$$E^{+}_{S} = E^{DFT}_{TS} - E^{DFT}_{vac} \quad (1)$$

where E^{DFT}_{TS} is the DFT energy of the TS and E^{DFT}_{vac} is the DFT energy of the vacancy state.

The 10 materials with the smallest S-NEB migration barriers go through the filter.

Climbing Image NEB

Climbing Image NEB (CI-NEB) is an extension to NEB, where the highest energy image is allowed to relax to the exact transition state.[29]

For the CI-NEB calculations the supercell from Figure 4(a) is used as the initial image, and by exchanging the positions of the vacancy and the X^+-ion in that structure, the final image is constructed. These are relaxed using the settings given in Structural Relaxations, omitting the initial rattling of atoms and relaxation of the unit cell. The same settings are used for the CI-NEB procedure, where the number of internal images is one

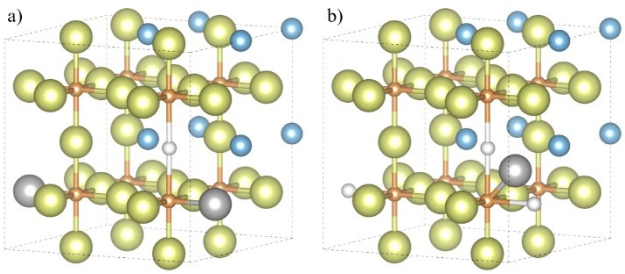

Figure 4. Illustration of the two supercell structures used in the S-NEB procedure. The color scheme is the same as in Figure 1 with the inclusion of white for the vacancies, and gray for the X-ion used for the TS, X^+. In a) the vacancy state is shown, whereas b) shows the TS.

© 2023 The Authors. Batteries & Supercaps published by Wiley-VCH GmbH

25666223, 2023, 6, Downloaded from https://chemistry-europe.onlinelibrary.wiley.com/doi/10.1002/batt.202300041 by University of Ulsan, Wiley Online Library on [11/11/2025]. See the Terms and Conditions (https://onlinelibrary.wiley.com/terms-and-conditions) on Wiley Online Library for rules of use; OA articles are governed by the applicable Creative Commons License

Research Article
doi.org/10.1002/batt.202300041
Chemistry Europe
European Chemical Societies Publishing

for Li and Na compounds and three for Mg compounds. The NEB implementation used is the standard ASE NEB with climbing image activated, and the Fast Inertial Relaxation Engine (FIRE) method was used as optimizer,[53] since the ASE CI-NEB implementation works best with this optimizer.

Nudged elastic band on charge density

The valence electron charge density (VASP CHGCAR) is used as a surrogate for the potential energy surface for the X-ion diffusion. The gradients of the potential surface are needed to perform the NEB on the potential, so (tri-)linear interpolation between the grid points is used to get these gradients. Our NEB implementation is based on the PyTorch-AutoNEB method published by Draxler et al.[54] The mechanical model, on which NEB is based, uses a chain of $N+2$ pivots (here, points in space) p_i for $i=\{0, \ldots, N+1\}$. The end point pivots, p_0 and p_{N+1}, are fixed, and all pivots are connected with springs with force constant k. A differentiable loss function $L(\cdot)$, for which we use the interpolated charge density, assigns a loss to each pivot. The potential energy of this system can be written as:

$$E(p) = \sum^{N}_{i=1} L(pi) + \sum^{N}_{i=0} 1/2\ k||p_{i+1} - p_i||^2 \quad (2)$$

The force on a pivot can be written as a sum of the loss function force and the spring forces:

$$F_i = -\nabla E(p) = F^{L}_{\ i} + F^{S}_{\ i} \quad (3)$$

Directly minimizing Equation (2) by moving p_i using the forces can cause corner cutting or sparse sampling of high energy regions with large and small k, respectively. Thus, in the NEB algorithm[55] the forces in Equation (3) are modified such that the loss force only acts perpendicular to the path and the spring forces only act parallel.

The number of points N and the force constant k are design parameters, and the choice of k is important, since the algorithm can become unstable if k is too large or converge slowly if it is too small.[54] To solve this, we follow the method of Draxler et al.[54] and redistribute the points along the path after each iteration, which is known as the string method.[56] For the estimation of the tangent vector $\hat{\tau}_i$ the implementation uses the improved method proposed by Henkelman and Jónsson,[57] improving stability around saddle points and reducing problems with kinked paths.[57]

The NEB path is initialized with 20 linearly interpolated points between the two vacancy positions. Optimization is fast, so the algorithm runs for 2000 steps using gradient steps with learning rate 0.5 and a momentum term of 0.1.

An example of the minimum charge density path is shown in Figure 5, with the X^+ position as a large green sphere.

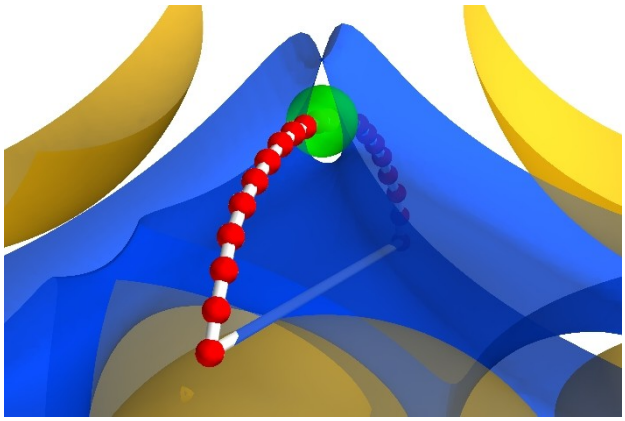

Figure 5. Minimum charge density path between two Li sites in Li_3OCl. The straight line shows the initial path. The connected red spheres show the final path and the points used in the NEB algorithm. The larger green sphere indicates the found TS position, X^+. Shown contours are the 38 and 160 meV/Å isosurfaces.

Results and Discussion

In this section we report and discuss the benchmark of the surrogate model used to predict migration barrier. Then we present the results of the filtering workflow employed to select a handful of antiperovskite compositions that score well on all the investigated parameters: thermodynamic and electrochemical stability, large band gap, and low migration barriers for charge carriers. From these results, the applicability of the S-NEB method is discussed.

Surrogate NEB

To examine the accuracy of the S-NEB method, we ran CI-NEB calculations for all the compounds that made it through to the ESW step in the workflow. These results are used to benchmark the S-NEB method, with 28 compounds examined, distributed as: 10 Li_3BA, 13 Na_3BA, and 5 Mg_3BA compounds.[1]

The magnitude of the S-NEB barriers was found to be larger than the CI-NEB barriers, so a scaling parameter, w, was introduced to allow comparison between the methods. The scaled barrier energies, $E^{\ddagger}$, are calculated as:

$$E^{\ddagger}_{i,j} = w_i \cdot E^{\ddagger}_{i,j} \quad (4)$$

where i indicates the barrier origin, either CD or S-NEB, and j indicates the compound.

A downside of introducing a scaling parameter is that the S-NEB method becomes better suited for ranking compounds based on barrier energy than direct estimation of barriers, since w must be estimated from a few NEB barriers. Herein, we have

[1] Li_3PHg, was excluded from this comparison, since the structure started decomposing during the CI-NEB relaxation, with a Hg-cluster forming in the supercell.

© 2023 The Authors. Batteries & Supercaps published by Wiley-VCH GmbH

25666223, 2023, 6, Downloaded from https://chemistry-europe.onlinelibrary.wiley.com/doi/10.1002/batt.202300041 by University of Ulsan, Wiley Online Library on [11/11/2025]. See the Terms and Conditions (https://onlinelibrary.wiley.com/terms-and-conditions) on Wiley Online Library for rules of use; OA articles are governed by the applicable Creative Commons License

Research Article
doi.org/10.1002/batt.202300041
Chemistry Europe
European Chemical Societies Publishing

optimized the scaling parameter using the absolute relative error, i.e.:

$$w_i = \min_{w' \in \mathbb{R}} \left(1/N \sum\nolimits_j^N \left|1 - w' E^{\ddagger}_{i,j} / E^{\ddagger}_{\mathrm{NEB},j}\right|\right) \quad (5)$$

Applied to the 28 compounds, the optimal value of the scaling parameter is $w_S = 0.470$.

As alluded to in the section Surrogate NEB, we get two estimates for the barrier height from the S-NEB procedure, the charge density barrier, denoted CD, and the S-NEB barrier itself. Based on other work,[34,36,37,58] our initial assumption was that the CD barriers would show some correlation towards the CI-NEB barriers. As seen in Figure 6 this seems not to be the case with the CD barriers, as they are almost constant for each X-ion. This is especially visible for the Na_3BA and Mg_3BA groups, where a linear trend line is close to horizontal.

Given the trend of the S-NEB data in Figure 6, there is a much stronger correlation between the scaled S-NEB barriers and the CI-NEB barriers, with a single scaling value able to fit quite well all examined X-ions.

The intended usage of the S-NEB method is ranking compounds based on the barrier estimate. Thus, in general there is no need to "calibrate" the weight against CI-NEB calculations, but clearly the method gives decently small errors when scaled, as seen in Table 1. Additionally, the S-NEB method is computationally much cheaper than CI-NEB. Based on the 28 data points, S-NEB is 10–30 times faster per internal image used by CI-NEB.

The deviation showing up for the Mg_3BA compounds is believed to arise from these compounds breaking the underlying assumption of the model, that the mobile ions can be treated as fully charged point charges.

Since the energy barriers for both S-NEB and CI-NEB is the energy difference between two configurations – the migrating atom at the initial lattice point and the TS – the source of discrepancies must come from differences in atomic coordinates between the two methods.

As seen in Figure 7, we have examined two measures of the differences, both between the TS of S-NEB and CI-NEB. We have omitted examining the differences of the initial structures, since the TS is the least stable configuration of the two, so should influence the error the most.

The first measure, denoted Transition State Displacement (TSD), is the distance between the TS ion, $X^{\ddagger}$, of the TSs of S-NEB and CI-NEB. It is shown on the x-axis of Figure 7. The other measure, denoted Average Structural Displacement (ASD), is the mean of the pair-wise distances between atoms in the two structures, which is shown as the coloring of each data point.

The structures are not aligned for the calculation of either measure, since one structure is relaxed to the bulk, the other to the TS. Therefore, any uniform translation or rotation of the atoms in the supercell impacts the displacements.

The error, plotted in Figure 7, shows a linear trend as a function of the TSD for low to medium displacements. When the ASD is high, deviations from this linear trend arise with no obvious trend. Thus, the difference in position of $X^{\ddagger}$ between S-NEB and CI-NEB has a large influence on the barrier energy, as to be expected, but a general discrepancy in the atomic positions between the two leads to an unpredictable difference between the energy barriers. The trend line not resulting in zero relative error at zero TSD is simply an artifact of the

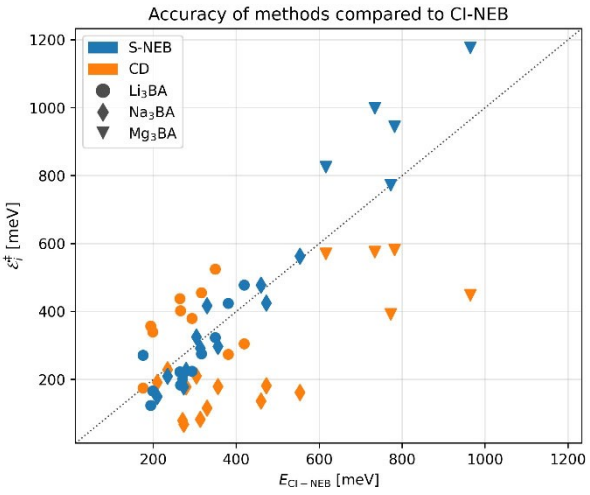

Figure 6. The barrier energies found using S-NEB and the accompanying charge density barrier, plotted against the CI-NEB barriers. The S-NEB and charge density barriers are scaled using Equation (4) with optimal weights of $w_S = 0.470$ and $w_{CD} = 7.55 \times 10^3$.

Table 1. The mean absolute error (MAE), standard deviation (SD) of errors, and mean relative error (MRE) between barrier energies calculated by S-NEB and CI-NEB.

Compound	MAE [meV]	SD [meV]	MRE [%]
Li_3BA	56	58	22
Na_3BA	49	47	17
Mg_3BA	171	91	23
All	73	96	20

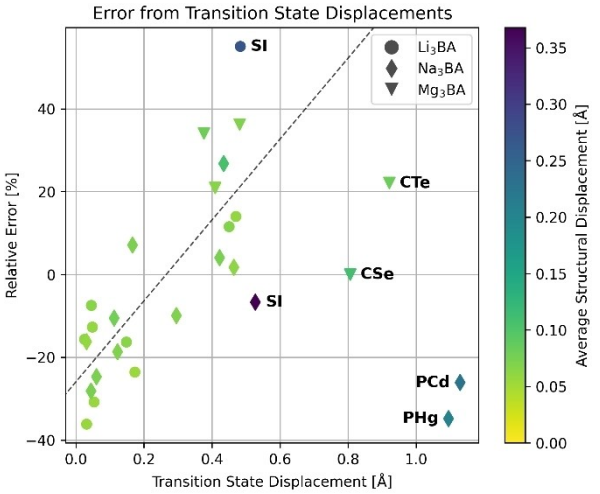

Figure 7. The relative error between S-NEB and CI-NEB as a function of the distance between $X^{\ddagger}$ in the TSs. The colors indicate the average pair-wise displacement of atoms between the TS for the methods. The labeled points are those identified as outliers from the linear trend.

© 2023 The Authors. Batteries & Supercaps published by Wiley-VCH GmbH

25666223, 2023, 6, Downloaded from https://chemistry-europe.onlinelibrary.wiley.com/doi/10.1002/batt.202300041 by University of Ulsan, Wiley Online Library on [11/11/2025]. See the Terms and Conditions (https://onlinelibrary.wiley.com/terms-and-conditions) on Wiley Online Library for rules of use; OA articles are governed by the applicable Creative Commons License

optimization function, Equation (5), since that uses no information about the TSD and ASD of the data points.

The outliers from the linear trend are highlighted in Figure 7. Examination of the charge density of these outlying compounds reveals that the cause is a breach in the assumption of the structure of the charge density. As shown in Figure 8, the charge density structure changes from having a closed loop inside the unit cell to an open area that terminates at the unit cell edge. Thus, X^{+} is incorrectly found in-between the B-atoms since the minimum charge density is instead at the unit cell edge.

The X^{+} position is defined by the relative charge density contributions from the A- and B-atom; a large charge density contribution has a repulsive effect on the path. Thus, the path ends up at the unit cell edge when the charge density contribution from the B-atom is much larger than from the A-atom, causing the S-NEB method to fail.

Examination of the charge density of all the compounds accepted by the criteria described in Antiperovskite Structure Check, shows that the compounds most prone to S-NEB model failure are those that have P, B, or C as the B-atom (76%, 74% and 41% of the examined compounds with that B-atom, respectively). For the other B-site atoms, the model failure rate is maximum 15%, with most of the failure happening for the Mg_3BA compounds. This higher failure rate of Mg compounds can possibly be attributed to non-perfect point charge behavior due to its +2 charge. If this is the case, that can limit the usability of the S-NEB method to only monovalent migrating ions. Thus, the promising divalent ions could be out of reach for this methodology.[59]

Visual inspection of the 28 compounds showed model failure for only the 4 already identified as outliers in Figure 7.

Workflow Results

The number of compounds rejected by each criterion of the workflow are shown in Figure 3. The structural check following the initial relaxation removed 502 candidates, corresponding to 38%. Thus, a decent number of compounds are more stable in other related space groups than in Pm-3m, while some of the rejections (~50) were due to the relaxations not being able to reach the set force criteria.

The convex hull criteria removed another 701 candidates, corresponding to 86%, so a very large proportion of the chemical space was rejected due to insufficient thermodynamic stability. The band gap criteria then rejected an additional 85 compounds, corresponding to 75%, leaving just 29 for examination of electrochemical stability.

Upon examining the composition of the compounds rejected by the first three steps, the inability of compositions to allow charge neutrality of the unit cell was the largest cause of rejection. Due to the restriction of using group I and II elements for the X-ion, the A- and B-ions must be able to balance the positive charge. This excludes many of the transition metals from ever making stable compounds, since the 5-atom unit cell disallows mixed oxidation states of the A and B-ions. The inability of the convex hull criteria to reject more of the compounds could be caused by the employed method. The convex hull computation is based on the Materials Project database, which gives no guarantee that the phase diagram for a given chemical system is complete. Thus, some compounds could make it past the convex hull criteria due to missing species in the database.

The compounds accepted by the band gap criteria are charge neutral with group 16 and 17 elements for A- and B-ions for Li_3BA and Na_3BA, and either only group 15 or groups 14 and 16 for Mg_3BA. This aligns nicely with what has been found earlier for perovskites.[60] Two classes of exceptions were identified, both slightly exotic.

Class I contains Li_3PHg, Na_3PCd and Na_3PHg, which can only be charge neutral, since P can accommodate 10 valence electrons. Then, since Cd and Hg are d^{10} metals, they are still very stable after losing their two outermost *s*-electrons to P. That no other elements, which can easily lose two electrons, have been found with P as the B-ion might be due to a strict requirement on the ionic radii of the A-ion, which only Cd and Hg seem to fulfill. This requirement could hint at an analogue to the Goldschmidt tolerance factor.[61] Class II contains the d^8 noble metals Pd and Pt, with Pt present in both hydrides and fluorides with Li and Na, while Pd is only found in Li_3FPd. That both metals acquire filled *s*- and *d*-orbitals, when accepting two electrons, could explain why they can appear in an effectively −2 oxidation state.

None of these compounds are electrochemically stable to any usable degree, with class I showing ESWs of 0.05–0.15 V, and class II showing ESWs of 0.01–0.46 V with the two lithium platinates being the most stable. Thus, even though these exotic compositions survive many of the initial criteria, they are ultimately deemed unusable due to poor electrochemical stability.

Only 14 of the 29 compounds accepted by the band gap criteria have an electrochemical stability window which is large enough to be considered for further analysis.

The compounds that were accepted by every criterion up to the S-NEB barrier can be seen in Table 2, where the calculated values for all properties are shown. The results

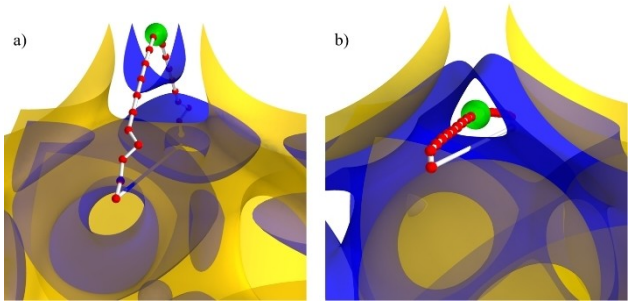

Figure 8. Charge density and optimized path for a) Na_3PCd, and b) Li_3FSe. a) Failure of the S-NEB method, where the TS has been incorrectly identified very near the edge of the unit cell. b) Success of the method with a properly identified TS, seen by the fully formed loop in the charge density. Settings used are like Figure 5.

© 2023 The Authors. Batteries & Supercaps published by Wiley-VCH GmbH

25666223, 2023, 6, Downloaded from https://chemistry-europe.onlinelibrary.wiley.com/doi/10.1002/batt.202300041 by University of Ulsan, Wiley Online Library on [11/11/2025]. See the Terms and Conditions (https://onlinelibrary.wiley.com/terms-and-conditions) on Wiley Online Library for rules of use; OA articles are governed by the applicable Creative Commons License

Research Article
doi.org/10.1002/batt.202300041
Chemistry Europe
European Chemical Societies Publishing

Table 2. The 14 candidates that made it to the Surrogate NEB step in Figure 3, ordered by X-ion and calculated CI-NEB barrier. The compounds in italic are the ones not in the top 10. A weight of $w_S = 0.470$ is used for scaling E^+_S.

	E_{hull} [eV/at]	Gap [eV]	ESW [V]	E^+_S [meV]	E^+_{NEB} [meV]
Li_3SI	0.195	3.7	2.52	272	175
Li_3FSe	0.057	3.8	2.13	124	194
Li_3Fte	0.065	3.0	1.58	166	198
Li_3Hse	0.017	3.6	1.01	184	265
Li_3Hte	0.012	3.1	1.03	224	293
Li_3OcI	0.145	4.9	2.86	424	380
Li_3Obr	0.157	4.5	2.80	478	419
Na_3Fse	0.044	2.0	1.58	227	279
Na_3SI	0.172	2.5	2.01	292	313
Na_3OcI	0.139	2.0	1.73	418	329
Na_3Fte	0.022	2.1	1.40	298	355
Na_3Obr	0.138	1.9	1.85	478	459
Na_3OI	0.138	2.0	1.15	563	553
Mg_3Nas	0.053	1.3	1.21	826	616

confirm both experimental and computational studies,[14,62–66] with all but the fluorides, Na_3OI, and Mg_3NAs having been synthesized. This does impact the novelty of the current work negatively, but is a strong argument for employing workflows, such as the one described here, as they are clearly able to discover compounds as effectively as researchers with area knowledge.

Experimental data relevant for this work is very sparse for these synthesized compounds with an ESW only measured for only Li3SI of 10 V[62] and extrapolated migration barriers only stated for Li3SI (0.29 eV) and Li3FSe (0.18 eV).[62,64]

The large difference in ESW is possibly due to kinetic inhibition of the decomposition, which is not included in the GPPD method, since it is based solely on thermodynamics.

The calculated migration barrier for Li_3SI is 0.12 eV too low, which could be explained by the rather large re-organization of the structure during migration. Curiously, the S-NEB barrier is much closer to the experimental. For Li_3FSe, the calculated and experimental barrier are much closer.

The materials that were not in the top 10, based on the S-NEB estimate of the barrier, are marked with italic in Table 2. Both the S-NEB method and CI-NEB identify the same 10 compounds as the best, even though the order of the ranking is slightly different. This highlights the usefulness of electrostatics-based methods as a part of accelerated workflows, since they can rank compounds quite well for a fraction of the cost.

Conclusions

In this study, we have used a filtering workflow, together with an accelerated method for migration barriers, to identify candidate SSEs. The candidates found have all been identified by other work, which would indicate that there are no new SSE candidates to be found in the Pm-3m space group with the compositions examined herein. However, this speaks to the applicability of this filtering computational workflow, since it was able to quickly identify many compounds that researchers have spent years discovering.

The accelerated method used for migration barriers, the surrogate model denoted S-NEB, shows several advantages for screening studies and high-throughput workflows in comparison to ordinary NEB. One advantage is the time usage, since the S-NEB method is 10–30 times faster than CI-NEB for each internal NEB image used. When the S-NEB method is used for screening, it can either be used directly for ranking of compounds based on migration barriers, or one can perform a few CI-NEBs to determine the S-NEB scaling factor, which gives a more direct measure of the barriers. Either way, a significant speed up can be expected compared to performing NEB on all candidates. Another advantage of S-NEB lies in the ability to reuse the charge density from the initial SCF calculation for all the migrations of interest, since any path in the unit or supercell can be optimized from the same charge density. Therefore, the investigation of migrations in mixed composition systems in various atomic configurations can be performed at a relatively small computational cost. Such a workflow can be further expedited by using linear scaling machine learning methods for charge density calculation[67] instead of relying on DFT. One of the weaknesses of the S-NEB method is that it is limited by the species present in the structure it is applied to. As seen in the results section, some elements alter the charge density such that the path minimization fails. These elements provide charge too far from the atoms, which affects the charge density such that the method is rendered unusable. In this study, we have found this issue to be prominent with P, B or C present.

The barriers obtained directly from the charge density are not very useful. This mostly comes from the inability to determine a zero-point for the barriers, as the static charge density obtained from the SCF calculation does not give insight into the change in charge density as the X-ion moves along the optimized migration path. This is the main reason, why the SCF calculations of the vacancy and TS super cells were instead used, but does not align with the successes of other methods that estimate barrier heights using the charge density.[34,36,37,58]

This work has only examined Li, Na, and Mg as X-ion, but both K and Ca could also be of interest as charge carriers. These could have been examined in this work, but the charge density must show a clear migration path like in Figure 5 to apply S-NEB, which we found not to be the case for at least Ca, since it has a residual partial charge. This caused the charge density barriers to have large flat valleys in the middle of the path instead of a localized peak as seen for the Li, Na, and Mg-cases, which made identification of the TS impossible.

Data Availability

The data, following the Data Management Plan of the BIG-MAP project,[68] that support the findings of this study are openly available in Materials Cloud.[69]

© 2023 The Authors. Batteries & Supercaps published by Wiley-VCH GmbH

25666223, 2023, 6, Downloaded from https://chemistry-europe.onlinelibrary.wiley.com/doi/10.1002/batt.202300041 by University of Ulsan, Wiley Online Library on [11/11/2025]. See the Terms and Conditions (https://onlinelibrary.wiley.com/terms-and-conditions) on Wiley Online Library for rules of use; OA articles are governed by the applicable Creative Commons License

Code Availability

The code will be made available on the BIG-MAP App Store (ESW determination), and on GitHub/-Lab (S-NEB method).

Acknowledgements

The authors acknowledge support from the EU's Horizon 2020 research and innovation program under grants agreement No 957189 (BIG-MAP) and No 957213 (BATTERY 2030PLUS). BHS and IEC acknowledge support from the Independent Research Fund Denmark (Research Project 1, project "Rational Design of High-Entropy Oxides for Protonic Ceramic Fuel Cells", grant number No 1032-00269B). PBJ and AB acknowledges financial support from VILLUM FONDEN (DeepDFT project, research grant No 00023105).

Conflict of Interest

The authors declare no competing interests.

Keywords: antiperovskites · density functional calculations · high-throughput screening · solid state electrolytes · surrogate model

[1] R. Chen, Q. Li, X. Yu, L. Chen, H. Li, *Chem. Rev.* **2020**, *120*, 6820–6877.
[2] P. Albertus, V. Anandan, C. Ban, N. Balsara, I. Belharouak, J. Buettner-Garrett, Z. Chen, C. Daniel, M. Doeff, N. J. Dudney, B. Dunn, S. J. Harris, S. Herle, E. Herbert, S. Kalnaus, J. A. Libera, D. Lu, S. Martin, B. D. McCloskey, M. T. McDowell, Y. S. Meng, J. Nanda, J. Sakamoto, E. C. Self, S. Tepavcevic, E. Wachsman, C. Wang, A. S. Westover, J. Xiao, T. Yersak, *ACS Energy Lett.* **2021**, *6*, 1399–1404.
[3] M. A. Kraft, S. Ohno, T. Zinkevich, R. Koerver, S. P. Culver, T. Fuchs, A. Senyshyn, S. Indris, B. J. Morgan, W. G. Zeier, *J. Am. Chem. Soc.* **2018**, *140*, 16330–16339.
[4] F. Zheng, M. Kotobuki, S. Song, M. O. Lai, L. Lu, *J. Power Sources* **2018**, *389*, 198–213.
[5] W. D. Richards, L. J. Miara, Y. Wang, J. C. Kim, G. Ceder, *Chem. Mater.* **2015**, *28*, 266–273.
[6] T. Famprikis, P. Canepa, J. A. Dawson, M. S. Islam, C. Masquelier, *Nat. Mater.* **2019**, *18*, 1278–1291.
[7] P. G. Bruce, A. R. West, *J. Electrochem. Soc.* **1983**, *130*, 662–669.
[8] Y. Zhu, X. He, Y. Mo, *ACS Appl. Mater. Interfaces* **2015**, *7*, 23685–23693.
[9] H. Aono, E. Sugimoto, Y. Sadaoka, N. Imanaka, G. ya Adachi, *J. Electrochem. Soc.* **1989**, *136*, 590–591.
[10] M. Itoh, Y. Inaguma, W. Jung, L. Chen, T. Nakamura, *Solid State Ionics* **1994**, *70–71*, 203–207.
[11] P. Knauth, *Solid State Ionics* **2009**, *180*, 911–916.
[12] B. Put, P. M. Vereecken, A. Stesmans, *J. Mater. Chem. A* **2018**, *6*, 4848–4859.
[13] V. Thangadurai, W. Weppner, *J. Am. Ceram. Soc.* **2005**, *88*, 411–418.
[14] K. Kim, D. J. Siegel, *Chem. Mater.* **2021**, *33*, 2187–2197.
[15] Y. Wang, Q. Wang, Z. Liu, Z. Zhou, S. Li, J. Zhu, R. Zou, Y. Wang, J. Lin, Y. Zhao, *J. Power Sources* **2015**, *293*, 735–740.
[16] Y. Wang, H. Zhang, J. Zhu, X. Lü, S. Li, R. Zou, Y. Zhao, *Adv. Mater.* **2019**, *32*, 1905007.
[17] J. Zheng, B. Perry, Y. Wu, *ACS Mater. Au* **2021**, *1*, 92–106.
[18] M. Oudah, A. Ikeda, J. N. Hausmann, S. Yonezawa, T. Fukumoto, S. Kobayashi, M. Sato, Y. Maeno, *Nat. Commun.* **2016**, *7*, 13617.
[19] A. Iyo, I. Hase, H. Fujihisa, Y. Gotoh, S. Ishida, H. Ninomiya, Y. Yoshida, H. Eisaki, H. T. Hirose, T. Terashima, K. Kawashima, *Inorg. Chem.* **2021**, *60*, 18017–18023.
[20] Ö. Çakır, E. Dias, K. R. Priolkar, A. Hoser, M. Farle, M. Acet, *Phys. Rev. B* **2020**, *102*, 024431.
[21] K. Takenaka, K. Asano, M. Misawa, H. Takagi, *Appl. Phys. Lett.* **2008**, *92*, 011927.
[22] P.-F. Li, Y.-Y. Tang, W.-Q. Liao, P.-P. Shi, X.-N. Hua, Y. Zhang, Z. Wei, H. Cai, R.-G. Xiong, *Angew. Chem. Int. Ed.* **2018**, *57*, 11939–11942; *Angew. Chem.* **2018**, *130*, 12115–12118.
[23] D. D. Vaughn II, J. Araujo, P. Meduri, J. F. Callejas, M. A. Hickner, R. E. Schaak, *Chem. Mater.* **2014**, *26*, 6226–6232.
[24] Y. Zhao, L. L. Daemen, *J. Am. Chem. Soc.* **2012**, *134*, 15042–15047.
[25] K. Alberi, M. B. Nardelli, A. Zakutayev, L. Mitas, S. Curtarolo, A. Jain, M. Fornari, N. Marzari, I. Takeuchi, M. L. Green, M. Kanatzidis, M. F. Toney, S. Butenko, B. Meredig, S. Lany, U. Kattner, A. Davydov, E. S. Toberer, V. Stevanovic, A. Walsh, N.-G. Park, A. Aspuru-Guzik, D. P. Tabor, J. Nelson, J. Murphy, A. Setlur, J. Gregoire, H. Li, R. Xiao, A. Ludwig, L. W. Martin, A. M. Rappe, S.-H. Wei, J. Perkins, *J. Phys. D* **2018**, *52*, 013001.
[26] Z. Deng, V. Kumar, F. T. Bölle, F. Caro, A. A. Franco, I. E. Castelli, P. Canepa, Z. W. Seh, *Energy Environ. Sci.* **2022**, *15*, 579–594.
[27] F. T. Bölle, N. R. Mathiesen, A. J. Nielsen, T. Vegge, J. M. Garcia-Lastra, I. E. Castelli, *Batteries & Supercaps* **2020**, *3*, 488–498.
[28] L. Kahle, A. Marcolongo, N. Marzari, *Energy Environ. Sci.* **2020**, *13*, 928–948.
[29] G. Henkelman, B. P. Uberuaga, H. Jónsson, *J. Chem. Phys.* **2000**, *113*, 9901–9904.
[30] N. R. Mathiesen, H. Jónsson, T. Vegge, J. M. G. Lastra, *J. Chem. Theory Comput.* **2019**, *15*, 3215–3222.
[31] F. T. Bölle, A. Bhowmik, T. Vegge, J. M. G. Lastra, I. E. Castelli, *Batteries & Supercaps* **2021**, *4*, 1516–1524.
[32] J. H. Chang, P. B. Jørgensen, S. Loftager, A. Bhowmik, J. M. G. Lastra, T. Vegge, *Electrochim. Acta* **2021**, *388*, 138551.
[33] O.-P. Koistinen, F. B. Dagbjartsdóttir, V. Ásgeirsson, A. Vehtari, H. Jónsson, *J. Chem. Phys.* **2017**, *147*, 152720.
[34] L. Kahle, A. Marcolongo, N. Marzari, *Phys. Rev. Mater.* **2018**, *2*, 065405.
[35] J.-X. Shen, H. H. Li, A. C. Rutt, M. K. Horton, K. A. Persson, **2022**, DOI 10.48550/arXiv.2202.00222.
[36] N. E. R. Zimmermann, D. C. Hannah, Z. Rong, M. Liu, G. Ceder, M. Haranczyk, K. A. Persson, *J. Phys. Chem. Lett.* **2018**, *9*, 628–634.
[37] Y. Liu, X. Jiang, J. Zhao, M. Hu, *Comput. Mater. Sci.* **2021**, *192*, 110380.
[38] J. Mortensen, M. Gjerding, K. Thygesen, *J. Open Source Software* **2020**, *5*, 1844.
[39] A. H. Larsen, J. J. Mortensen, J. Blomqvist, I. E. Castelli, R. Christensen, M. Dułak, J. Friis, M. N. Groves, B. Hammer, C. Hargus, E. D. Hermes, P. C. Jennings, P. B. Jensen, J. Kermode, J. R. Kitchin, E. L. Kolsbjerg, J. Kubal, K. Kaasbjerg, S. Lysgaard, J. B. Maronsson, T. Maxson, T. Olsen, L. Pastewka, A. Peterson, C. Rostgaard, J. Schiøtz, O. Schütt, M. Strange, K. S. Thygesen, T. Vegge, L. Vilhelmsen, M. Walter, Z. Zeng, K. W. Jacobsen, *J. Phys. Condens. Matter* **2017**, *29*, 273002.
[40] G. Kresse, J. Furthmüller, *Phys. Rev. B* **1996**, *54*, 11169–11186.
[41] G. Kresse, D. Joubert, *Phys. Rev. B* **1999**, *59*, 1758–1775.
[42] I. E. Castelli, T. Olsen, S. Datta, D. D. Landis, S. Dahl, K. S. Thygesen, K. W. Jacobsen, *Energy Environ. Sci.* **2012**, *5*, 5814–5819.
[43] J. P. Perdew, K. Burke, M. Ernzerhof, *Phys. Rev. Lett.* **1996**, *77*, 3865–3868.
[44] A. Jain, S. P. Ong, G. Hautier, W. Chen, W. D. Richards, S. Dacek, S. Cholia, D. Gunter, D. Skinner, G. Ceder, K. A. Persson, *APL Mater.* **2013**, *1*, 011002.
[45] S. P. Ong, L. Wang, B. Kang, G. Ceder, *Chem. Mater.* **2008**, *20*, 1798–1807.
[46] S. P. Ong, A. Jain, G. Hautier, B. Kang, G. Ceder, *Electrochem. Commun.* **2010**, *12*, 427–430.
[47] W. Sun, S. T. Dacek, S. P. Ong, G. Hautier, A. Jain, W. D. Richards, A. C. Gamst, K. A. Persson, G. Ceder, *Sci. Adv.* **2016**, *2*, e1600225.
[48] V. Esposito, I. E. Castelli, *Adv. Mater. Interfaces* **2020**, *7*, 1902090.
[49] I. E. Castelli, F. Hüser, M. Pandey, H. Li, K. S. Thygesen, B. Seger, A. Jain, K. A. Persson, G. Ceder, K. W. Jacobsen, *Adv. Energy Mater.* **2014**, *5*, 1400915.
[50] Y. Mo, S. P. Ong, G. Ceder, *Chem. Mater.* **2011**, *24*, 15–17.
[51] A. Emly, E. Kioupakis, A. V. der Ven, *Chem. Mater.* **2013**, *25*, 4663–4670.
[52] T. Binninger, A. Marcolongo, M. Mottet, V. Weber, T. Laino, *J. Mater. Chem. A* **2020**, *8*, 1347–1359.
[53] E. Bitzek, P. Koskinen, F. Gähler, M. Moseler, P. Gumbsch, *Phys. Rev. Lett.* **2006**, *97*, 170201.
[54] F. Draxler, K. Veschgini, M. Salmhofer, F. A. Hamprecht, *Proceedings of the 35th International Conference on Machine Learning*, Vol. 80, PMLR **2018**, 1309–1317.

© 2023 The Authors. Batteries & Supercaps published by Wiley-VCH GmbH

25666223, 2023, 6, Downloaded from https://chemistry-europe.onlinelibrary.wiley.com/doi/10.1002/batt.202300041 by University of Ulsan, Wiley Online Library on [11/11/2025]. See the Terms and Conditions (https://onlinelibrary.wiley.com/terms-and-conditions) on Wiley Online Library for rules of use; OA articles are governed by the applicable Creative Commons License

[55] H. Jónsson, G. Mills, K. W. Jacobsen, *Classical and Quantum Dynamics in Condensed Phase Simulations*, (Eds: B. J. Burne, G. Ciccotti, D. F. Coker), World Scientific **1998**, 385–404.
[56] D. Sheppard, R. Terrell, G. Henkelman, *J. Chem. Phys.* **2008**, *128*, 134106.
[57] G. Henkelman, H. Jónsson, *J. Chem. Phys.* **2000**, *113*, 9978–9985.
[58] Z. Rong, D. Kitchaev, P. Canepa, W. Huang, G. Ceder, *J. Chem. Phys.* **2016**, *145*, 074112.
[59] M. Sotoudeh, A. Gross, *JACS Au* **2022**, *4*, 463–471.
[60] I. E. Castelli, K. W. Jacobsen, *Modell. Simul. Mater. Sci. Eng.* **2014**, *22*, 055007.
[61] V. M. Goldschmidt, *Naturwissenschaften* **1926**, *14*, 477–485.
[62] R. Rajagopal, M.-H. Park, Y. Subramanian, Y. J. Jung, K.-S. Ryu, *J. Electroanal. Chem.* **2021**, *895*, 115477.
[63] L. Yin, M. Murphy, K. Kim, L. Hu, J. Cabana, D. J. Siegel, S. H. Lapidus, *Inorg. Chem.* **2020**, *59*, 11244–11247.
[64] S. Fujii, S. Gao, C. Tassel, T. Zhu, T. Broux, K. Okada, Y. Miyahara, A. Kuwabara, H. Kageyama, *J. Am. Chem. Soc.* **2021**, *143*, 10668–10675.
[65] K. Kim, D. J. Siegel, *J. Mater. Chem. A* **2019**, *7*, 3216–3227.
[66] S. Gao, T. Broux, S. Fujii, C. Tassel, K. Yamamoto, Y. Xiao, I. Oikawa, H. Takamura, H. Ubukata, Y. Watanabe, K. Fujii, M. Yashima, A. Kuwabara, Y. Uchimoto, H. Kageyama, *Nat. Commun.* **2021**, *12*, 201.
[67] P. B. Jørgensen, A. Bhowmik, *npj Comput. Mater.* **2022**, *8*, 183.
[68] I. E. Castelli, D. J. Arismendi-Arrieta, A. Bhowmik, I. Cekic-Laskovic, S. Clark, R. Dominko, E. Flores, J. Flowers, K. U. Frederiksen, J. Friis, A. Grimaud, K. V. Hansen, L. J. Hardwick, K. Hermansson, L. Königer, H. Lauritzen, F. L. Cras, H. Li, S. Lyonnard, H. Lorrmann, N. Marzari, L. Niedzicki, G. Pizzi, F. Rahmanian, H. Stein, M. Uhrin, W. Wenzel, M. Winter, C. Wölke, T. Vegge, *Batteries & Supercaps* **2021**, *4*, 1803–1812.
[69] B. H. Sjølin, P. B. Jørgensen, A. Fedrigucci, T. Vegge, A. Bhowmik, I. E. Castelli, *Accelerated Workflow for Antiperovskite-based Solid State Electrolytes*, Materials Cloud Archive **2022**, DOI 10.24435/materialscloud:39-xs.

Manuscript received: February 3, 2023
Revised manuscript received: March 24, 2023
Accepted manuscript online: March 30, 2023
Version of record online: April 27, 2023

© 2023 The Authors. Batteries & Supercaps published by Wiley-VCH GmbH

25666223, 2023, 6, Downloaded from https://chemistry-europe.onlinelibrary.wiley.com/doi/10.1002/batt.202300041 by University of Ulsan, Wiley Online Library on [11/11/2025]. See the Terms and Conditions (https://onlinelibrary.wiley.com/terms-and-conditions) on Wiley Online Library for rules of use; OA articles are governed by the applicable Creative Commons License